Supplementary Materials for

Probing the Ultimate Limits of Plasmonic Enhancement

C. Ciracì, R. T. Hill, J. J. Mock, Y. Urzhumov, A. I. Fernández-Domínguez, S. A. Maier,
J. B. Pendry, A. Chilkoti, and D. R. Smith

correspondence to: cristian.ciraci@duke.edu

This PDF file includes:

Materials and Methods
Supplementary Text
Figs. S1 to S2
References (20-25)

Materials and Methods:

Gold films and the molecular spacer layers with attached colloidal nanoparticles (NPs) were prepared and characterized in the following manner: 30 nm gold films were deposited by an electron beam evaporator (CHA Industries) at 2 Å/s onto clean room cleaned Nexterion Glass B slides (Schott North America, Inc.) using a 5 nm chromium adhesion layer (deposited at 1 Å/s). Poly-electrolyte (PE) spacer layers of up to 27 nm thickness were prepared by layer-by-layer (LBL) deposition (*18*) of poly (allylamine) hydrochloride (PAH, M_w = 70 kDa, Aldrich) and polystyrene sulfonate (PSS, M_w = 70 kDa, Aldrich). For each deposition step, the gold-coated glass slides were immersed in 0.003 moles-of-monomer/L (monomol/L) PE and 1 M NaCl for 30 min, rinsed thoroughly with a gentle stream of ultra-pure water (18 MΩ, used throughout), and immersed in fresh ultra-pure water for one minute, after which the substrates were either immersed in 1 M NaCl for 30 s before repeating the same steps for deposition of the oppositely charged PE or dried with a stream of high-purity nitrogen for analysis. All LBL depositions were initiated and terminated with the cationic PAH layer to facilitate both the attachment of the first PE layer to the gold film through amine-gold interactions (*20*) and the electrostatic immobilization of gold nanoparticles to the PE spacer layer.

To create spacer layers with controllable thicknesses from just a few angstroms to a few nanometers, self-assembled monolayers (SAMs) of amine-terminated alkanethiols on gold films were fabricated using using chain lengths of n = 2, 3, 6, 8, 11, and 16 where n equals the number of carbon atoms along the alkane portion of the molecule. Amine thiols of n = 2, 3, 6, and 11 were purchased from Sigma-Aldrich (product numbers 30070, 739294, 733679, and 674397 respectively), and amine thiols of n = 8 and 16 were purchased from Dojindo (product numbers A424 and A458 respectively). All thiols were used as received. The SAMs were fabricated by incubating a gold slide that was either fresh from the metal evaporator or had been stored in 200 proof ethanol since gold deposition in a clean glass vial containing a 1-5 mM thiol solution in 200 proof ethanol for 18 hours, after which the vials were briefly sonicated and copiously rinsed with ethanol a total of 4 times. Finally, the gold-coated glass slides containing the SAMs were removed from ethanol and were dried with a stream of high-purity nitrogen.

60 nm gold NPs (BBI) were electrostatically immobilized on the top surfaces of each molecular spacer layer by incubating a volume of un-diluted colloid stock solution on the molecular spacer layer for 30 minutes, followed by rinsing with ultra-pure water and drying with a stream of high purity nitrogen. Resultant NP surface coverages ranged from 1-3 scatterers/ μm^2, which ensured that there was minimal NP-NP coupling.

Film-coupled NP gap distances are assumed to be set by the molecular spacer thickness. We assume here that the loosely bound citrate molecules that serve as stabilizers for the gold colloid are displaced by the amine groups (*21*) present on our molecular spacer layers due to amine-gold interactions (*20*). PE spacer layer thicknesses were measured using a J.A. Woolam Co., Inc., M-88 spectroscopic ellipsometer and WVASE32 software (version 3.460). Spectroscopic scans (277.5 – 763 nm) of each spacer layer were performed in three distinct regions (free of immobilized NPs) at 65°, 70°, and 75° relative to the normal of the surface of the slide. Ellipsometry data was

analyzed using a 2-layer model (*22*) composed of a bulk gold layer underneath an organic layer, which was used to represent the molecular layer. The thickness of each spacer layer was fitted using the Cauchy expression for a normal dispersion provided by the WVASE32 software, where parameters "Thickness" and "A" of the model were fitted (all other variables were left at the default values) such that the mean standard error of the fit was minimized. For each spacer layer, the nominal thickness was determined to be the average of the three thickness measurements taken per spacer layer. Note that the optical constants of each bare gold film were determined immediately prior to LBL depositions by taking spectroscopic scans of the bare gold films at 65°, 70°, and 75° and fitting *n* and *k* to the known values of bulk gold, which were provided by the WVASE32 software, to account for any shifts in the optical constants due to the thicknesses of our gold films. These fitted optical constants for each gold slide were saved and used later, respectively, when fitting for thickness of the molecular layers deposited onto the gold slides.

Ellipsometry was also used to characterize the thinner amine thiol spacer layers using the same procedure described above except for the fact that only "Thickness" (and not "A") was fitted in the Cauchy model. We found that fitting A produced unrealistic thickness and A values and assumed this was due to the lack of contrast between the extremely thin molecular layers and the gold film. Even so, we were unable to obtain fitted thickness values for our thinnest C2 amine thiol layers using ellipsometry. Furthermore, we found that extrapolation of the ellipsometry thickness data produced unreasonably thin values for the C2 layers. This is supported by the findings of Bain *et al.* (*19*) who made similar characterizations of series of alkane thiol and carboxy-terminated alkane thiol SAMs and show how ellipsometry of thin molecular layers can produce systematically low thickness values. To come up with useable thickness values for the amine thiol SAMs, we used a 3D chemical modeling program (Chem3D Pro 7.0) to generate the theoretical lengths of each amine thiol attached to a gold atom via a thiolate bond. The molecular lengths were measured from the gold atom (representing the gold film surface) to the most distant hydrogen atom of the terminal amine group as if the molecule was standing straight up on the gold surface. We then calculated the chain lengths of the molecules as if they were tilted by 30° relative to the normal of the surface since it is commonly accepted that SAM formation of thiols on gold surfaces results in thiol molecules assuming some degree of tilt (*19*). These tilted length values were used in our final plots of NP resonant scattering data versus NP-film separation distance (Fig. 4D). Our measured ellipsometric thickness data produced slopes and intercepts ranging from 1.6 – 2.0 Å/carbon and -6.0 – -0.9 Å when all values of n are included. However, when the C16 points are removed from the regression, the slopes and intercepts were 1.1 – 1.4 Å/carbon and -2.5 – 4.4 Å. These slope values are more similar to the theoretical values. It should be expected that the slope of such a range of n might not be constant in reality since longer chain lengths of thiols tend to form more ordered and well-packed SAMs.   Our ellipsometric data seems similar to the case of Ref. (*19*), where the ellipsometric thickness versus thiol chain length data produced somewhat reasonable slope values, compared to theoretical data, but unrealistic y-intercepts.

Plasmon resonances of gold film-coupled NPs were characterized by scattering spectra, reflectivity spectra, and color images. Scattering spectra and images were taken using a customized Nikon dark-field microscope with a 100x DF 0.9 NA objective.

Slides containing the gold films with spacer layers and immobilized NPs were index-matched with oil to the top surface of a hemi-cylindrical lens, which we use in place of a prism. Samples were illuminated from above, in dark-field mode, using un-polarized white light from a 75 W Xenon lamp (Oriel). For color images, the microscope light path was directed to a Nikon d90 color camera. Scattering spectra were acquired using a 1mm image plane pinhole aperture to reduce the field of view to ~10μm diameter, containing small numbers of NPs, which enables the user to remove unwanted scattering from contaminants (typically dust) in the spectroscopy path. This field of view was directed through a spectrometer (Acton SpectraPro 2300i) and onto a detector (Photometrics CoolSnap HQ). All scattering spectra were background corrected (by subtracting the spectrum from an apertured region of the substrate containing no NPs) and normalized (by dividing the spectrum from a white scattering standard (Labsphere)) to correct for the wavelength response of the imaging system. To measure the reflectance properties of the samples, white light from a 75 W Xenon source (Oriel) coupled through a 1 mm diameter multimode optical fiber, collimating lens and p-polarizer is directed to the sample surface at a 70° angle of incidence. The beam diameter at the surface of the sample is approximately 3 mm. The reflected light is collected through a second identical lens fiber assembly and directed to the spectrometer where the spectrum is normalized by the reflectance spectrum of the bare gold film. Plasmon resonance peak positions are calculated by taking the centroid of the resonances observed in either the scattering or the reflectivity curves.

Supplementary Text:

Hydrodynamic model

The electromagnetic nonlocal response of metal can be described by a hydrodynamic model (*11*). The electron fluid density, $n(\mathbf{r}, t)$, and the current density, $\mathbf{J} = en\mathbf{v}$, satisfy the Euler's equation:

$$m_e n\left[\frac{\partial \mathbf{v}}{\partial t} + (\mathbf{v} \cdot \nabla)\mathbf{v}\right] + \gamma m_e n\mathbf{v} = en\mathbf{E} + en\mathbf{v} \times \mathbf{B} - \nabla p , \qquad (S1)$$

along with the continuity equation:

$$\nabla \cdot \mathbf{J} = -e\dot{n} , \qquad (S2)$$

where m_e is the free electron mass, γ is the electron collision rate, $\mathbf{v}$ is the electron velocity field and p is the electron pressure which for a three-dimensional gas, may be expressed as:

$$p(\mathbf{r},t) = p_0\left[\frac{n(\mathbf{r},t)}{n_0}\right]^{5/3} , \qquad (S3)$$

with $p_0 \propto n_0 E_F$, (E_F is the Fermi energy and n_0 is the equilibrium charge density). Combining Eqs. (S1), (S2) and (S3), and neglecting higher order terms, one finds that the free electron current $\mathbf{J}$ satisfies the following equation:

$$-\beta^2 \nabla(\nabla \cdot \mathbf{J}) + \frac{\partial^2}{\partial t^2} \mathbf{J} + \gamma \frac{\partial}{\partial t} \mathbf{J} = \frac{n_0 e^2}{m_e} \frac{\partial}{\partial t} \mathbf{E}, \tag{S4}$$

with $\beta \propto \sqrt{E_F / m_e}$. This equation describes the electromagnetic response of a metal and must be solved along with Maxwell's equations. In the framework of harmonic propagation, we get then the following system of two coupled equations:

$$\nabla \times \nabla \times \mathbf{E} - k_0^2 \mathbf{E} = i\omega\mu_0 \mathbf{J}, \tag{S5}$$

$$\beta^2 \nabla(\nabla \cdot \mathbf{J}) + (\omega^2 + i\gamma\omega)\mathbf{J} = i\omega\omega_p^2 \varepsilon_0 \mathbf{E}, \tag{S6}$$

with $\omega_p = \sqrt{\dfrac{n_0 e^2}{\varepsilon_0 m_e}}$.

The presence of spatial derivatives in the description of the current vector requires the specifications of new boundary conditions—additional boundary conditions (ABCs)—to solve the electromagnetic problem given by the Eqs. (S5) and (S6). In the frame of a hydrodynamic description, the number of ABCs depends on the given equilibrium charge density profile at the metal boundaries. In writing Eq. (S4) we implicitly assumed the equilibrium electron density to have a step function profile that vanishes outside the metal. In this case, only one ABC is required to supplement Eqs. (S5) and (S6) to obtain a unique solution (23). However, the choice of the ABC required at the metal interface is a delicate problem that remains an unsettled topic in the literature. In our calculations we assume a all-nonlocal metal permittivity. In this case, we can unambiguously impose the continuity of the normal component of the electric field, which corresponds to the condition:

$$\hat{\mathbf{n}} \cdot (\mathbf{J} - \mathbf{J}_d) = 0 \tag{S7}$$

at the boundary, with $\mathbf{J}_d$ denoting the displacement currents flowing through the dielectric. The ABC of Eq. (S7) reduces to $\hat{\mathbf{n}} \cdot \mathbf{J} = 0$ for a metal-vacuum interface.

Analytical calculations: film-coupled nanowire

In order to provide additional physical insight on the film-coupled nanoparticle system, as well as an independent confirmation of our numerical treatment of nonlocal effects, we present an analytical description of the system based on transformation optics (TO) (8). We focus our attention on the two-dimensional analogue of the experimental structure, a metal nanowire on top of a flat metal substrate. The local TO description of this system maps the original structure into a flat metal-air-metal geometry (24). This is possible through the conformal transformation:

$$z' = \ln\left(\frac{g}{z} + 1\right), \tag{S8}$$

where $z' = x' + iy'$ and $z = x + iy$ are transformed and original spatial coordinates, respectively. The constant $g = 4R\sqrt{\rho(1+\rho)}$ gives the transformation length scale, where

$\rho = \delta / 2R$ is the ratio between the gap size and the nanowire diameter. The thickness of the air slab between the metal regions in the transformed frame is given by $a = 2\mathrm{asinh}\left(\sqrt{\rho}\right)$. Figure S1 shows a schematic representation of the original and transformed structures as well as a definition of the different geometric parameters. Equation (S8) does not only act on the geometry of the plasmonic device, but also on the external excitation. It maps the original incident field into a periodic array of dipole sources placed at the surface of one of the transformed metal surfaces. Importantly, the periodic character of the transformed source converts the continuum spectrum of parallel wave-vectors into a discrete set of Bloch wave orders.

Whereas the material properties are preserved under the transformation within the local approximation, the metal permittivity becomes sensitive to Eq. (S8) once spatial dispersion is taken into account (8). The transverse component of the metal permittivity, $\varepsilon_T(\omega)$, described by a local Drude-like expression, is not affected by the conformal mapping. On the other hand, the longitudinal component, $\varepsilon_L(k,\omega)$, given by Eq. (2), is modified through the wave-vector stretching associated to Equation (S8) and weighted by $|dz'/dz|$. The nonlocal parameter β acquires a spatial dependence, having:

$$\beta' = \beta'(z') = \frac{2\beta}{g}\left|\cosh z' - 1\right|, \tag{S9}$$

in the transformed frame. Equation (S9) translates into the spatial variation of the Thomas-Fermi screening length, $\lambda'_{\mathrm{TF}}(z') \approx \beta'(z')/\omega_p$. This effect is illustrated in Fig. S1, where the shaded areas represent the decay length of the longitudinal plasmons (surface charge thicknesses) excited in the structure.
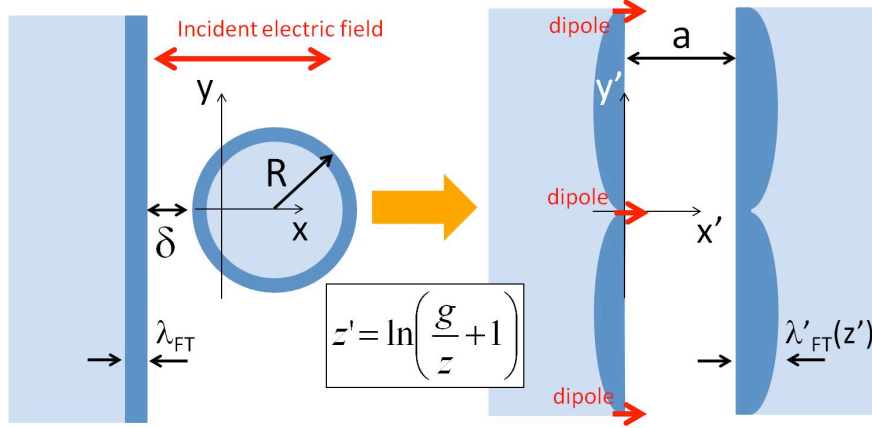
Fig. S1: Left panel renders the two-dimensional system under study: the interaction of light with a metal nanowire of radius R separated by a gap δ from a flat metal substrate. The right panel shows the geometry obtained from the original under the transformation given by Eq. (S8). The shaded areas in both panels represent the Thomas-Fermi screening length (decay length of the longitudinal plasmons excited in the system).

We restrict our analysis to the low frequency (large wavelength) gap plasmonic mode, and study the dependence of the mode wavelength on the nanowire-substrate distance. The parallel wave-vector for this mode is given by the lowest order Bloch wave, which corresponds to a single electric field oscillation along the y'-direction within unit cell of the transformed structure. This greatly simplifies the analytical treatment of the spatial dependence of the nonlocal parameter given by Eq. (S9).

Taking advantage of the fact that the length scale in which $\beta'(z')$ varies is much smaller than the inverse of the parallel wave-vector for the longest wavelength plasmonic mode, we can replace Eq. (S9) by its average along the y'-direction. Using this approximate treatment, the resonance condition for the longest wavelength plasmonic mode can be calculated, yielding:

$$\left(\sqrt{\rho}+\sqrt{\rho+1}\right)^4 = \mathrm{Re}\left\{\frac{\varepsilon_T(\omega)-1}{\varepsilon_T(\omega)\frac{q_0-1}{q_0+1}+1}\frac{\varepsilon_T(\omega)-1}{\varepsilon_T(\omega)\frac{q_a-1}{q_a+1}+1}\right\}, \tag{S10}$$

where:

$$q_0 = \sqrt{1+\frac{\omega_P^2-\omega^2}{\beta'(0)^2}} = \sqrt{1+\left(\frac{2R}{\beta}\right)^2\frac{\rho(\rho+1)}{(1-2/\pi)^2}\left(\omega_P^2-\omega^2\right)}, \tag{S11}$$

$$q_a = \sqrt{1+\frac{\omega_P^2-\omega^2}{\beta'(a)^2}} = \sqrt{1+\left(\frac{2R}{\beta}\right)^2\frac{\rho(\rho+1)}{(2\rho+1-2/\pi)^2}\left(\omega_P^2-\omega^2\right)}, \tag{S12}$$

are the x'-component of the longitudinal plasmons wave-vector in $x'\leq 0$ (transformed substrate) and $x'\geq a$ (transformed nanowire) metallic regions.

Figure S2 shows a comparison of analytical results given by Eq. (S10) with numerical simulations obtained by directly solving the system of Eqs. (S5) and (S6) with COMSOL Multiphysics. The resonant wavelength is computed for a cylinder of radius R=10 nm placed over an infinitely extend metal substrate at various gap distances δ. In the numerical model, the resonances are driven by a p-polarized plane wave incoming at 75° from normal. The system resonances are evaluated by integrating the total power dissipation density over the cross-section of the cylinder. Let us stress that Eq. (S10) fails to describe accurately the resonant position in two limits. On the one hand, the approximate treatment of the spatially dependent nonlocal parameter in Eq. (S9) is not valid for gap sizes much smaller than the Thomas-Fermi wavelength ($\delta < \beta/\omega_p \approx 0.1$ nm in all the cases considered in Fig. S2). On the other hand, as mentioned above, Eq. (S10) does not take into account the contribution of higher energy gap modes to the optical response of the structure. These overlap with the fundamental resonance when the gap size becomes comparable to the nanowire diameter ($\delta > 1$ nm in Fig. S2). Finally, analytical results agree with numerical simulations in the region where the assumption made are valid, giving us an independent confirmation of our results. Though the numerical implementation of nonlocality for a full three-dimensional system remains unchanged from its 2D analogy, the same direct calculation would require in this case extremely large computational resources. In the next section we introduce a quasi-two-dimensional modeling method that allows a sensible reduction of the computational load.
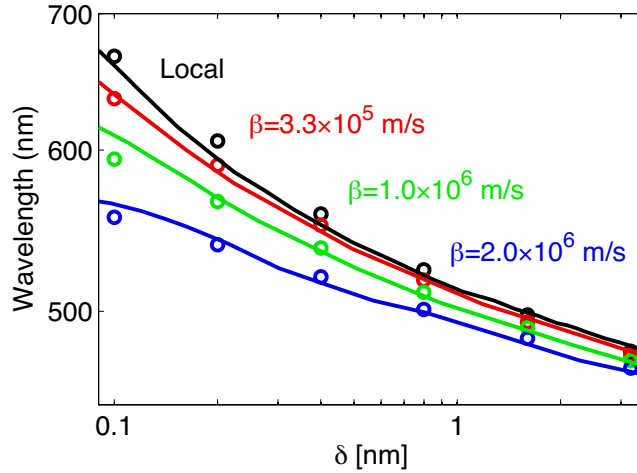
Fig. S2: Comparison of analytical with numerical results. The resonant wavelength is plotted as a function of the gap distance δ for a cylinder of radius R=10 nm placed over an infinitely extend metal substrate. Analytical calculations (solid line) and numerical simulations (circles) were performed for different values of the nonlocal parameter β. The curve obtained using the local approximation is shown in black.

Simulations: 2.5D model

Numerical investigations of near-fields and scattering properties of the film-coupled NP system were performed solving the system of Eqs. (S5) and (S6) in COMSOL Multiphysics. In order to sensibly decrease the computational load we have developed a quasi-two-dimensional modeling method for vector fields, which will be referred as *2.5D modeling*. In the 2.5D formulation, all fields are decomposed in term of azimuthal mode number m. This can be done by decomposing the fields into the Fourier series:

$$E_{\rho,z,\phi}(\rho,z,\phi) = \sum_m E_{\rho,z,\phi}^{(m)}(\rho,z)e^{im\phi}. \qquad (S13)$$

If the geometry is ϕ-independent, i.e. it is rotationally symmetric, each cylindrical harmonic propagates independently, and the full vector equations can be solved on the two-dimensional cross-section of the simulation domain for each m.

In order to solve properly the electromagnetic problem, it is then necessary to modify the built-in Comsol master equation, as well as the built-in boundary condition equation. The new equations can be easily obtained substituting the expression (S13) (and similar expressions for **J**) in the Eq. (S5) in cylindrical coordinates. After eliminating the ϕ-dependence, the equations depend on the azimuthal number m, and have to be solved for each cylindrical harmonic present in the incident field. Fortunately, parity condition relating positive and negative azimuthal number exists, which further reduces the computational load by a factor of two. In general, parity condition depends on the particular field component considered. Total 3D fields can be obtained by revolution around z-axis by reintroducing the ϕ-dependent factor, $e^{im\phi}$.

All excitations can be decomposed as follow. Consider a plane wave polarized such that the magnetic field is transverse to the z-axis (TM$_z$ polarization), i.e. $H_z = 0$ and

$$\mathbf{E} = E_0\left(\hat{\mathbf{x}}\cos\theta + \hat{\mathbf{z}}\sin\theta\right)e^{-ik_0 x\sin\theta}e^{ik_0 z\cos\theta}. \tag{S14}$$

Taking advantage from the periodicity with respect to ϕ of the part depending on $x = \rho\cos\phi$ it is possible to expand the z-component of $\mathbf{E}$ as Fourier series:

$$E_z = E_0\sin\theta e^{ik_0 z\cos\theta}\sum_m i^{-m}J_m\left(k_0\rho\sin\theta\right)e^{im\phi}. \tag{S15}$$

Using Maxwell's equations it is possible to derive all remaining field components:

$$E_\phi = i\frac{\cos\theta}{k_0\rho\sin\theta}E_0 e^{ik_0 z\cos\theta}\sum_m mi^{-m+1}J_m\left(k_0\rho\sin\theta\right)e^{im\phi}, \tag{S16}$$

$$E_\rho = iE_0\cos\theta e^{ik_0 z\cos\theta}\sum_m i^{-m}J'_m\left(k_0\rho\sin\theta\right)e^{im\phi}, \tag{S17}$$

As already mentioned, it is necessary to calculate the fields only on a cross-section of the three-dimensional geometry. The simulated domain then reduces to a disc of radius 2 µm. The excitation is a plane wave p-polarized and incident at an angle $\theta = 75°$ from the normal to the film.

In order to collect the field scattered from the nanoparticle, we used a generalized scattered-field formulation, in which the background field is specified using an analytical formula for the structure in absence of the nanoparticle. For the background field, we used Fresnel formulas for a layered system consisting of a semi-infinite layer of air (refractive index $n = 1$), a flat layer for the polymer, 30 nm thick layer of metal, and a semi-infinite layer of glass ($n = 1.47$). For each layer, the background field is then a superposition of two plane waves, which are decomposed into cylindrical harmonics by means of Eqs. (S13). The resonant wavelength is obtained in correspondence of the maximum in the scattering cross-section. This is obtained by integrating the scattered power flow over a range of spherical angles corresponding to the experimental numerical aperture NA = 0.9 (NA = $n_{air}\sin\theta_{max}$).

In the local approximation, we used for gold, wavelength-dependent permittivity interpolating Johnson & Christy data (25). In order to get nonlocal data independently on the particular choice of Drude parameters in Eq. (S6), we proceeded as follow. Equation (S6) may be rewritten as:

$$\frac{\beta^2}{\omega_p^2}\nabla(\nabla\cdot\mathbf{J}) + \frac{\omega^2 + i\gamma\omega}{\omega_p^2}\mathbf{J} = i\omega\varepsilon_0\mathbf{E}. \tag{S18}$$

Recognizing that $\varepsilon_D(\omega) = 1 - \dfrac{\omega_p^2}{\omega^2 + i\gamma\omega}$, we can write:

$$\frac{\beta^2}{\omega_p^2}\nabla(\nabla\cdot\mathbf{J}) - \frac{1}{\varepsilon_D(\omega) - 1}\mathbf{J} = i\omega\varepsilon_0\mathbf{E}. \tag{S19}$$

It is still possible then, to use an arbitrary frequency-dependent dielectric function, $\varepsilon(\omega)$, to describe gold properties within the nonlocal model. As in the local approximation we used a dielectric function obtained by interpolating Johnson & Christy data (25).

Additional Author notes: